Dispersion analysis of spectral element methods for elastic wave propagation

G. Seriani [a,*], S.P. Oliveira [b]

[a] *Istituto Nazionale di Oceanografia e Geofisica Sperimentale, Borgo Grotta Gigante, 42/c, Sgonico (TS) 34010, Italy*
[b] *Centro de Pesquisa em Geofísica e Geologia, Campus Universitário de Ondina, Salvador, BA 40170-115, Brazil*

Abstract

We study the numerical dispersion of spectral element methods of arbitrary order for the isotropic elastic wave equation in two and three dimensions by a simplified modal analysis of the discrete wave operators. This analysis is based on a Rayleigh quotient approximation of the eigenvalue problem that characterizes the dispersion relation. This approximation takes full advantage of the tensor product representation of the spectral element matrices. We compute dispersion graphs that show the dependence of the phase/group velocity, the polarization error, and the numerical anisotropy on the grid resolution as well as the polynomial degree with both Gauss–Lobatto–Chebyshev and Gauss–Lobatto–Legendre collocation points.
© 2007 Elsevier B.V. All rights reserved.

1. Introduction

The spectral element method has become an established technique in the field of computational seismology. This high-order numerical technique combines the high accuracy of spectral methods with the flexibility of finite elements and takes advantage of parallel computer architectures.

Spectral elements were originally applied to fluid dynamics [20] and became popular for wave propagation because they were able to deliver low numerical dispersion with respect to standard finite element methods [19,25]. In this work, we study the accuracy of spectral elements for the elastic wave equation. The spectral element method for elastic wave propagation is well known for quadrilateral meshes with shape functions based on Chebyshev [21] or Legendre [11] orthogonal polynomials, as well as for triangular grids [16]. However, no theoretical analysis of the accuracy of spectral elements for elastic media is available in the literature [3].

Marfurt [14], Zyserman and Gauzellino [27] have studied the numerical dispersion of 2D and 3D linear finite element methods. They plug a harmonic plane wave into the finite element stencil assuming an infinite,

---

* Corresponding author.
E-mail addresses: gseriani@inogs.it (G. Seriani), saulopo@cpgg.ufba.br (S.P. Oliveira).

periodic mesh. For higher-order methods, the numerical dispersion relation found by this strategy is expressed by an eigenvalue problem where the eigenvalues and eigenvectors represent the approximate angular frequencies and the amplitudes within an element, respectively. Marfurt [15] notices that most of these eigenvalues poorly approximate the exact angular frequencies for each wave number and refer to them as *parasitic* modes.

In the present work we estimate the numerical angular frequency by writing the finite element solution as a harmonic plane wave, as in the classical analysis (see Appendix C for a short review of the classical approach and the main motivations for the present approach). We do not consider amplitude changes within an element; that is, we want to find an eigenvalue associated to a fixed vector. This vector corresponds to the plane wave sampled in the grid nodes. In general, this eigenvalue does not exist. We consider then its best approximation, which is the Rayleigh quotient associated to the sampled plane wave. The Rayleigh quotient is unique, so parasitic modes are not an issue. We have used this methodology for the dispersion analysis of the acoustic wave equation [24] and in the design of spectral element operators with improved accuracy [23].

For the sake of simplicity, we focus on the isotropic elastic wave equation. In the following, we consider Cartesian grids, for which the spectral element matrices are represented as tensor products of 1D element matrices. Then, we substitute the harmonic plane wave sampled in the grid nodes into the system of equations arising from the spatial discretization. We compute the Rayleigh quotient approximation of the resulting eigensystem, which can be computed in an efficient way by using a reduced number of operations. From the Rayleigh quotient we compute estimates of phase/group velocity and polarization errors. We illustrate these estimates with spectral element methods based on Chebyshev and Legendre collocation points. In particular, we confirm the rule of thumb that eighth-degree spectral elements require about four grid points per wavelength for an accurate simulation.

2. The isotropic elastic wave equation

The isotropic elastic wave equation is given by

$$\rho \ddot{\boldsymbol{u}} - (\lambda + \mu)\nabla(\nabla \cdot \boldsymbol{u}) - \mu\nabla \cdot \nabla\boldsymbol{u} = 0, \tag{1}$$

where $\ddot{\boldsymbol{u}} = \partial^2\boldsymbol{u}/\partial t^2$, $\lambda, \mu > 0$ are the Lamé coefficients and $\rho > 0$ is the density. The elastic modulus and the Poisson's ratio for isotropic media are $E := \lambda + 2\mu$ and $v := \lambda/2(\lambda + \mu)$, respectively.

To study the dispersion of numerical schemes for the wave equation (1), it is convenient to consider particular solutions $\boldsymbol{u}[\boldsymbol{\kappa}](\boldsymbol{x}, t) := \boldsymbol{R}\exp[-\mathrm{i}(\omega t - \boldsymbol{\kappa} \cdot \boldsymbol{x})]$, which are known as harmonic plane waves. The parameters ω and $\boldsymbol{\kappa}$ are the angular frequency and the wavevector, respectively, while $\boldsymbol{R}$ is the direction of particle movement. Following [9], the solution $\boldsymbol{u}[\boldsymbol{\kappa}]$ satisfies (1) if

$$\left(\frac{\omega^2}{\kappa^2} - c_S^2\right)\boldsymbol{R} + \left(c_P^2 - c_S^2\right)\left(\boldsymbol{R} \cdot \frac{\boldsymbol{\kappa}}{\kappa}\right)\frac{\boldsymbol{\kappa}}{\kappa} = \boldsymbol{0}, \tag{2}$$

where $\kappa := |\boldsymbol{\kappa}|$ and

$$c_P := \sqrt{\frac{\lambda + 2\mu}{\rho}}, \quad c_S := \sqrt{\frac{\mu}{\rho}}. \tag{3}$$

The vector equation (2) admits the solutions $(\omega_P, \boldsymbol{R}_P)$ and $(\omega_S, \boldsymbol{R}_S)$ in two dimensions. We have the dispersion relations $\omega_P = \kappa c_P$ and $\omega_S = \kappa c_S$, while the amplitudes $\boldsymbol{R}_P$ and $\boldsymbol{R}_S$ satisfy the following polarity relations:

$$\boldsymbol{R}_P = \left(\boldsymbol{R}_P \cdot \frac{\boldsymbol{\kappa}}{\kappa}\right)\frac{\boldsymbol{\kappa}}{\kappa}, \quad \boldsymbol{R}_S \cdot \frac{\boldsymbol{\kappa}}{\kappa} = 0. \tag{4}$$

These solutions are related to waves that travel with velocities c_P and c_S. The wave field with velocity c_P induces a displacement $\boldsymbol{u}_P$ in the same direction as the wave vector $\boldsymbol{\kappa}$ and it is called a compressional wave or P-wave. On the other hand, the wave field with velocity c_S is called a shear wave (S-wave) and it induces a displacement $\boldsymbol{u}_S$ perpendicular to $\boldsymbol{\kappa}$.

In three dimensions, Eq. (2) admits three solutions, defined by the dispersion relations $\omega_P = \kappa c_P$ and $\omega_{SV} = \omega_{SH} = \kappa c_S$; the amplitude $\boldsymbol{R}_P$ is in the direction of $\boldsymbol{\kappa}$ as in two dimensions, while $\boldsymbol{R}_{SV}$ and $\boldsymbol{R}_{SH}$ are in the plane normal to $\boldsymbol{\kappa}$. We take $\boldsymbol{R}_{SV}$ in the (x_1, x_2)-plane and $\boldsymbol{R}_{SH} \perp \boldsymbol{R}_{SV}$. The solutions with angular

frequencies ω_{SV} and ω_{SH} are related to the vertically polarized (SV-) and horizontally polarized (SH-) waves, respectively.

3. Spectral element approximation

We consider Cartesian grids of square and cubic elements, as in the classical dispersion analysis. Let us initially partition the 1D domain $[0, 1]$ into n_e equally spaced elements of size $h := 1/n_e$ subdivided into N interior subintervals, so that the total number of nodes is $\mathcal{N} := Nn_e$.

We index the elements by $0 \leqslant e \leqslant n_e - 1$, while the local index $0 \leqslant j \leqslant N - 1$ locates a node within an element. These two indices provide a global ordering of all grid nodes, which is given by $p := j + eN$. The grid coordinates are defined by $x[p] := (e + \zeta_j)h$, where ζ_j is the jth *collocation point* in the reference interval $[0, 1]$. We assume that the collocation points are symmetrically distributed with respect to the element midpoint, i.e.,

$$\zeta_j = 1 - \zeta_{N-j}. \tag{5}$$

We consider $\Omega := [0, 1] \times [0, 1]$ in 2D. The mesh is defined as a tensor product of the 1D mesh; that is, we have n_e^2 square elements with N^2 interior nodes. The coordinates of the mesh nodes are $(x_1[p_1], x_2[p_2])$,

$$x_\alpha[p_\alpha] := (e_\alpha + \zeta_{j_\alpha})h, \quad p_\alpha = j_\alpha + e_\alpha N. \tag{6}$$

The index $\alpha \in \{1, 2\}$ in 2D, while $\alpha \in \{1, 2, 3\}$ in 3D. Finite element computations often require a scalar index rather than an ordered pair of indices. For this purpose we introduce

$$e := e_1 + e_2 n_e, \quad j := j_1 + j_2 N, \quad p := p_1 + p_2 \mathcal{N}. \tag{7}$$

Such an ordering is motivated by the Kronecker (or tensor) product operator: the Kronecker product $C := A \otimes B$ of an $N_2 \times M_2$ matrix A and an $N_1 \times M_1$ matrix B is an $N_1 N_2 \times M_1 M_2$ matrix defined as $C_{p_1 + p_2 M_1, q_1 + q_2 M_2} := A_{p_2, q_2} B_{p_1, q_1}$.

For this particular grid, the Nth degree spectral element approximation of (1) can be written as the following system of equations [21]:

$$\begin{cases} M\ddot{u}_1^*(t) + K_1 u_1^*(t) + K_2 u_2^*(t) = 0 \\ M\ddot{u}_2^*(t) + K_2^T u_1^*(t) + K_3 u_2^*(t) = 0, \end{cases} \tag{8}$$

together with initial and boundary conditions. The unknowns of the linear system (8) are the vectors $u_1^*(t)$ and $u_2^*(t)$ with the nodal approximations of the exact solution $u(x, t) = (u_1(x, t), u_2(x, t))$, i.e., $(u_\alpha)_p(t) \approx u_\alpha(x[p], t)$ $(0 \leqslant p \leqslant \mathcal{N} - 1)$, while the matrices M and K_i $(i = 1, 2, 3)$ are assembled from the local matrices

$$\begin{aligned} M^e &:= \rho(h^2/4)A \otimes A, \\ K_1^e &:= EA \otimes B + \mu B \otimes A, \\ K_2^e &:= \lambda C^T \otimes C + \mu C \otimes C^T, \\ K_3^e &:= \mu A \otimes B + EB \otimes A, \end{aligned} \tag{9}$$

where the *elementary matrices* A, B, and C are defined as

$$A_{l,j} = \int_{-1}^{1} \varphi_j(z)\varphi_l(z)\,\mathrm{d}z, \quad B_{l,j} = \int_{-1}^{1} \frac{\partial \varphi_j}{\partial z}(z)\frac{\partial \varphi_l}{\partial z}(z)\,\mathrm{d}z, \quad C_{l,j} = \int_{-1}^{1} \varphi_j(z)\frac{\partial \varphi_l}{\partial z}(z)\,\mathrm{d}z, \tag{10}$$

with $0 \leqslant l, j \leqslant N$. The functions $\varphi_i(z)$ form the Lagrangian interpolant basis satisfying the relation $\varphi_i(\xi_j) = \delta_{ij}$ within $[-1, 1]$, where $\xi_j := 2\zeta_j - 1$. Two standard sets of collocation points are the Gauss–Lobatto–Legendre (GLL) and Gauss–Lobatto–Chebyshev (GLC) points.

The GLL points are found by numerically solving the equation $(1 - \xi^2)P_N'(\xi) = 0$, where P_N' denotes the derivative of the Legendre polynomial of degree N. The same collocation points are used for the numerical integration of the elementary matrices, which renders the mass matrix diagonal [11]. The GLC points are $\zeta_j := [1 - \cos(\pi j/N)]/2$; we compute the elementary matrices analytically with Chebyshev orthogonal polynomials [22].

The grid for $\Omega := [0, 1]^3$ is analogous: we have n_e^3 cubic elements with N^3 interior nodes. We define the scalar indices

$$e := e_1 + (e_2 + e_3 n_e)n_e, \quad j := j_1 + (j_2 + j_3 N)N, \quad p := p_1 + (p_2 + p_3 \mathcal{N})\mathcal{N}, \tag{11}$$

while the mesh coordinates $\boldsymbol{x}[p] := (x_1[p_1], x_2[p_2], x_3[p_3])$ are defined by (6) for $\alpha = 1, 2, 3$. The 3D version of the spectral element formulation (8) is given by

$$\begin{cases} \boldsymbol{M}\ddot{\boldsymbol{u}}_1^*(t) + \boldsymbol{K}_1\boldsymbol{u}_1^*(t) + \boldsymbol{K}_2\boldsymbol{u}_2^*(t) + \boldsymbol{K}_3\boldsymbol{u}_3^*(t) = \boldsymbol{0} \\ \boldsymbol{M}\ddot{\boldsymbol{u}}_2^*(t) + \boldsymbol{K}_2^{\mathrm{T}}\boldsymbol{u}_1^*(t) + \boldsymbol{K}_4\boldsymbol{u}_2^*(t) + \boldsymbol{K}_5\boldsymbol{u}_3^*(t) = \boldsymbol{0} \\ \boldsymbol{M}\ddot{\boldsymbol{u}}_3^*(t) + \boldsymbol{K}_3^{\mathrm{T}}\boldsymbol{u}_1^*(t) + \boldsymbol{K}_5^{\mathrm{T}}\boldsymbol{u}_2^*(t) + \boldsymbol{K}_6\boldsymbol{u}_3^*(t) = \boldsymbol{0}, \end{cases} \tag{12}$$

where the matrices $\boldsymbol{M}$ and $\boldsymbol{K}_i$ ($1 \leqslant i \leqslant 6$) are assembled from the local matrices listed in Appendix A.

4. Modal analysis

Let us write the approximate solution of the 2D equation in the form of a harmonic plane wave:

$$u_\alpha^*[\boldsymbol{\kappa}](\boldsymbol{x}[p], t) = R_\alpha^* \exp\left[\mathrm{i}(\boldsymbol{\kappa} \cdot \boldsymbol{x}[p] - \omega^* t)\right], \quad 0 \leqslant p \leqslant \mathcal{N}^2 - 1. \tag{13}$$

By substituting the plane wave into the continuum equation (1), we have that the exact parameters $\boldsymbol{R}$ and ω satisfy (2). Analogously, we substitute (13) into the discrete equation (8) to compute the approximate parameters $\boldsymbol{R}^*$ and ω^*. Such a substitution yields

$$\begin{cases} -R_1^*\chi\boldsymbol{M}\boldsymbol{W}[\boldsymbol{\kappa}] + R_1^*\boldsymbol{K}_1\boldsymbol{W}[\boldsymbol{\kappa}] + R_2^*\boldsymbol{K}_2\boldsymbol{W}[\boldsymbol{\kappa}] = \boldsymbol{0} \\ -R_2^*\chi\boldsymbol{M}\boldsymbol{W}[\boldsymbol{\kappa}] + R_1^*\boldsymbol{K}_2^{\mathrm{T}}\boldsymbol{W}[\boldsymbol{\kappa}] + R_2^*\boldsymbol{K}_3\boldsymbol{W}[\boldsymbol{\kappa}] = \boldsymbol{0}, \end{cases} \tag{14}$$

where $\chi := (\omega^*)^2$ and

$$\boldsymbol{W}[\boldsymbol{\kappa}] = \boldsymbol{W}[\kappa_2] \otimes \boldsymbol{W}[\kappa_1], \quad W_p[\kappa_\alpha] := \exp(\mathrm{i}\kappa_\alpha x_\alpha[p_\alpha]). \tag{15}$$

We write the transformed linear system (14) as a block eigenvalue problem $\boldsymbol{X}\boldsymbol{y} = \chi\boldsymbol{Z}\boldsymbol{y}$,

$$\boldsymbol{X} := \begin{bmatrix} \boldsymbol{K}_1 & \boldsymbol{K}_2 \\ \boldsymbol{K}_2^{\mathrm{T}} & \boldsymbol{K}_3 \end{bmatrix}, \quad \boldsymbol{y} := \begin{bmatrix} R_1^*\boldsymbol{W}[\boldsymbol{\kappa}] \\ R_2^*\boldsymbol{W}[\boldsymbol{\kappa}] \end{bmatrix}, \quad \boldsymbol{Z} := \begin{bmatrix} \boldsymbol{M} & 0 \\ 0 & \boldsymbol{M} \end{bmatrix}. \tag{16}$$

Note that the solution χ exists only if $\boldsymbol{y}$ is an eigenvector of $\boldsymbol{X}\boldsymbol{y} = \chi\boldsymbol{Z}\boldsymbol{y}$. This is not true in general because the plane wave sampled in the mesh nodes is not necessarily a solution of the spectral element equation (8). However, one can choose χ^* that best approximates the eigenvalue χ in the sense that the residual $(\boldsymbol{X} - \chi\boldsymbol{Z})\boldsymbol{y}$ is orthogonal to $\boldsymbol{y}$ [10]. The best approximation χ^* exists and is given by the Rayleigh quotient

$$\chi^* = \frac{\overline{\boldsymbol{y}}^{\mathrm{T}}\boldsymbol{X}\boldsymbol{y}}{\overline{\boldsymbol{y}}^{\mathrm{T}}\boldsymbol{Z}\boldsymbol{y}}, \tag{17}$$

where $\overline{\boldsymbol{y}}^{\mathrm{T}}$ is the conjugate transpose of $\boldsymbol{y}$. Eq. (17) is equivalent to solving the 2×2 eigenvalue problem

$$\begin{bmatrix} d_1 & d_2 \\ \bar{d}_2 & d_3 \end{bmatrix} \begin{bmatrix} R_1^* \\ R_2^* \end{bmatrix} = \chi^* \begin{bmatrix} R_1^* \\ R_2^* \end{bmatrix}, \quad d_i := \frac{\overline{\boldsymbol{W}[\boldsymbol{\kappa}]}^{\mathrm{T}}\boldsymbol{K}_i\boldsymbol{W}[\boldsymbol{\kappa}]}{\overline{\boldsymbol{W}[\boldsymbol{\kappa}]}^{\mathrm{T}}\boldsymbol{M}\boldsymbol{W}[\boldsymbol{\kappa}]}. \tag{18}$$

We show in Appendix B that the coefficients d_i are real numbers that depend only on the polynomial degree, the elementary matrices, and the collocation points. We approximate $(\omega^*)^2$ by χ^*, which has two solutions from (18). We associate the larger solution to the numerical P-wave and the smaller one to the numerical S-wave, i.e., $\omega_P^* = \sqrt{\chi_+^*}$ and $\omega_S^* = \sqrt{\chi_-^*}$, where

$$\chi_\pm^* = \frac{d_1 + d_3}{2} \pm \sqrt{\left(\frac{d_1 - d_3}{2}\right)^2 + d_2^2}. \tag{19}$$

The estimate (19) does not take into account boundary conditions. At this point we consider another assumption from classical dispersion analysis: the assumption that the mesh is unbounded and periodic. Since the coefficients d_i do not depend on n_e, we have that (19) remains valid if the number of elements tends to infinity. In this situation we have a homogeneous (hence periodic) unbounded mesh.

The eigenvectors $\boldsymbol{R}_{P,S}^*$ associated to $\omega_{P,S}^*$ are readily found from (18) and (19):

$$\boldsymbol{R}_P^* = \begin{bmatrix} (\omega_P^*)^2 - d_3 \\ d_2 \end{bmatrix}, \quad \boldsymbol{R}_S^* = \begin{bmatrix} d_2 \\ (\omega_S^*)^2 - d_1 \end{bmatrix}. \tag{20}$$

Since the eigenvalue problem (18) is symmetric, $\boldsymbol{R}_P^*$ is perpendicular to $\boldsymbol{R}_S^*$. Thus, the angle between $\boldsymbol{R}_P^*$ and $\boldsymbol{R}_P$,

$$\varepsilon_{\mathrm{Pol}} := \arccos\left(\frac{\boldsymbol{R}_P^* \cdot \boldsymbol{R}_P}{|\boldsymbol{R}_P^*||\boldsymbol{R}_P|}\right), \tag{21}$$

is the same as the angle between $\boldsymbol{R}_S^*$ and $\boldsymbol{R}_S$. We refer to $\varepsilon_{\mathrm{Pol}}$ as the *polarity error* of the scheme (8).

The 3D modal analysis is not significantly different than the 2D case. Substituting into each row of (12) a solution in the form

$$\boldsymbol{u}_\alpha^*[\boldsymbol{\kappa}](t) = R_\alpha^* \exp^{-\mathrm{i}\omega^* t} \boldsymbol{W}[\boldsymbol{\kappa}], \quad \boldsymbol{W}[\boldsymbol{\kappa}] = W[\kappa_3] \otimes W[\kappa_2] \otimes W[\kappa_1], \tag{22}$$

where each $W[\kappa_\alpha]$ is defined as in (15), we find the block eigenvalue problem $\boldsymbol{X}\boldsymbol{y} = \chi\boldsymbol{Z}\boldsymbol{y}$, where $\chi := (\omega^*)^2$ and

$$\boldsymbol{X} := \begin{bmatrix} \boldsymbol{K}_1 & \boldsymbol{K}_2 & \boldsymbol{K}_3 \\ \boldsymbol{K}_2^{\mathrm{T}} & \boldsymbol{K}_4 & \boldsymbol{K}_5 \\ \boldsymbol{K}_3^{\mathrm{T}} & \boldsymbol{K}_5^{\mathrm{T}} & \boldsymbol{K}_6 \end{bmatrix}, \quad \boldsymbol{y} := \begin{bmatrix} R_1^*\boldsymbol{W}[\boldsymbol{\kappa}] \\ R_2^*\boldsymbol{W}[\boldsymbol{\kappa}] \\ R_3^*\boldsymbol{W}[\boldsymbol{\kappa}] \end{bmatrix}, \quad \boldsymbol{Z} := \begin{bmatrix} \boldsymbol{M} & 0 & 0 \\ 0 & \boldsymbol{M} & 0 \\ 0 & 0 & \boldsymbol{M} \end{bmatrix}. \tag{23}$$

We approximate χ by the Rayleigh quotient of $\boldsymbol{X}\boldsymbol{y} = \chi\boldsymbol{Z}\boldsymbol{y}$, which also satisfies the real-valued, 3×3 eigenvalue problem

$$\begin{bmatrix} d_1 & d_2 & d_3 \\ d_2 & d_4 & d_5 \\ d_3 & d_5 & d_6 \end{bmatrix}\begin{bmatrix} R_1^* \\ R_2^* \\ R_3^* \end{bmatrix} = \chi^*\begin{bmatrix} R_1^* \\ R_2^* \\ R_3^* \end{bmatrix}, \quad d_i := \frac{\overline{\boldsymbol{W}[\boldsymbol{\kappa}]}^{\mathrm{T}}\boldsymbol{K}_i\boldsymbol{W}[\boldsymbol{\kappa}]}{\overline{\boldsymbol{W}[\boldsymbol{\kappa}]}^{\mathrm{T}}\boldsymbol{M}\boldsymbol{W}[\boldsymbol{\kappa}]}. \tag{24}$$

All eigenvalues of (24) are real [12], so we can find the roots of the characteristic polynomial with a simple exact formula [18]. Moreover, the eigenvalues associated to ω_{SH}^* and ω_{SV}^* are not necessarily the same, although this difference is negligible when the number of grid points per wavelength is large enough [27]. We choose the eigenvalue that produces the larger error, in order that the numerical dispersion curves exhibit the worst case.

Remark: The methodology above support time discretizations as well. For instance, consider the explicit, second-order finite difference approximation in time [11] of the system (8):

$$\begin{cases} \boldsymbol{M}\left[\boldsymbol{u}_1^*(t_{n+1}) - 2\boldsymbol{u}_1^*(t_n) + \boldsymbol{u}_1^*(t_{n-1})\right] + \Delta t^2\boldsymbol{K}_1\boldsymbol{u}_1^*(t_n) + \Delta t^2\boldsymbol{K}_2\boldsymbol{u}_2^*(t_n) = \boldsymbol{0} \\ \boldsymbol{M}\left[\boldsymbol{u}_2^*(t_{n+1}) - 2\boldsymbol{u}_2^*(t_n) + \boldsymbol{u}_2^*(t_{n-1})\right] + \Delta t^2\boldsymbol{K}_2^{\mathrm{T}}\boldsymbol{u}_1^*(t_n) + \Delta t^2\boldsymbol{K}_3\boldsymbol{u}_2^*(t_n) = \boldsymbol{0}. \end{cases}$$

Substituting the plane wave (13) evaluated at $t = t_n$ in the equation above and dividing by $\exp(-\mathrm{i}\omega^* t_n)$, we find the same equations as in (14), except that $\chi = (2\sin(\omega^*\Delta t/2)/\Delta t)^2$.

5. Numerical results

Let $\boldsymbol{\kappa} = 2\pi k(\cos\theta, \sin\theta)$ in 2D and $\boldsymbol{\kappa} = 2\pi k(\cos\theta\cos\phi, \sin\theta\cos\phi, \sin\phi)$ in 3D. We measure the grid resolution by the number of grid points per wavelength $G := \mathcal{N}/k$ or the normalized spatial frequency $H := k/\mathcal{N}$. We set $\rho = 2$ g/cm^3, $c_P = 3$ km/s, although the graphs below comprise dimensionless variables. The remaining elastic parameters are computed from ρ, c_P, and the Poisson's ratio v. We use $\mathcal{N} = 120$ nodes in 2D, $\mathcal{N} = 72$ in 3D, and choose the polynomial degree as $N = 4, 8, 12$.

From the numerical angular frequency ω_P^* we compute the numerical phase velocity $c_P^* = \omega_P^*/\kappa = \omega_P^*/(2\pi H \mathcal{N})$. We compute the numerical group velocity $\tilde{c}_P^*$ in the direction of $\boldsymbol{\kappa}$ by a central-difference approximation of the directional derivative of ω_P^*. Analogously, c_S^* and $\tilde{c}_S^*$ are evaluated from ω_S^*.

The modal analysis with Rayleigh quotients is consistent with the standard dispersion analysis for linear finite elements. Note from Fig. 1 that the 2D and 3D numerical dispersion coefficients $\tilde{c}_S^*/\tilde{c}_S$ computed as above match the curves found in [27,28], which are based on the standard analysis. We further compare both approaches in Appendix C.

Figs. 2–5 show the phase and group velocity errors

$$\varepsilon_P := \frac{c_P^* - c_P}{c_P}, \quad \tilde{\varepsilon}_P := \frac{\tilde{c}_P^* - \tilde{c}_P}{c_P}, \quad \varepsilon_S := \frac{c_S^* - c_S}{c_S}, \quad \tilde{\varepsilon}_S := \frac{\tilde{c}_S^* - \tilde{c}_S}{c_S}$$

of the eighth-degree spectral element method with GLC and GLL collocation points. We set the axes to emphasize the interval where the error is below 1%. The errors are below this limit until $H \approx 0.25$, i.e., four points per wavelength. The difference between spectral element methods with GLL and GLC points is because the GLC formulation employs a consistent mass formulation, while the GLL employs a diagonal mass formulation. In particular, the GLL approach tends to produce lagging error, as in classical lumped formulations [4], except in Fig. 3(b) and Fig. 5(b). Note also in these figures that the error curves with $\theta = 30°$ and $v = 0.4$ nearly coincide with the error curves with $\theta = 45°$ and $v = 0.1$.

Fig. 6 shows the P-wave phase error of the eighth-degree GLC and GLL spectral element methods with the second-degree explicit time integration scheme and confirms that low-order time discretizations deteriorate the high accuracy in space. We define the stability parameter with respect to the P-wave velocity, i.e., $\text{CFL} = c_P \Delta t \mathcal{N}$. The time-harmonic case is indicated by $\text{CFL} = 0$.

Let us set $\theta = 0°$ and study the dependence of the 2D dispersion error on the polynomial degree (Figs. 7 and 8). At this particular direction (in which P- and S-wave velocity errors coincide), two differences between consistent and diagonal formulations are evident. First, GLC produces leading error, while GLL produces lagging error. Moreover, the GLC error is higher along the axes, while the same is not necessarily true for GLL spectral elements, as also observed for consistent and lumped approximations of the acoustic wave equation [4]. Note also that Fig. 8 is consistent with the theoretical evidence that the spectral element method preserves optimal convergence with respect to N [2,13].

The polarity error (21) does not depend on the Poisson's ratio, as also noticed in [14]. Fig. 9 shows the 2D polarity errors for several polynomial degrees for wave vectors defined by $\theta = 30°$. The polarization error of the eighth-degree method is negligible also when the number of grid points per wavelength is greater than or equal to four.

Fig. 10 shows the variation with the Poisson's ratio of the minimum number of grid point per wavelength needed to keep the 2D group errors below 1% [14]. We consider the polynomial degrees $N = 4, 8, 12$. The
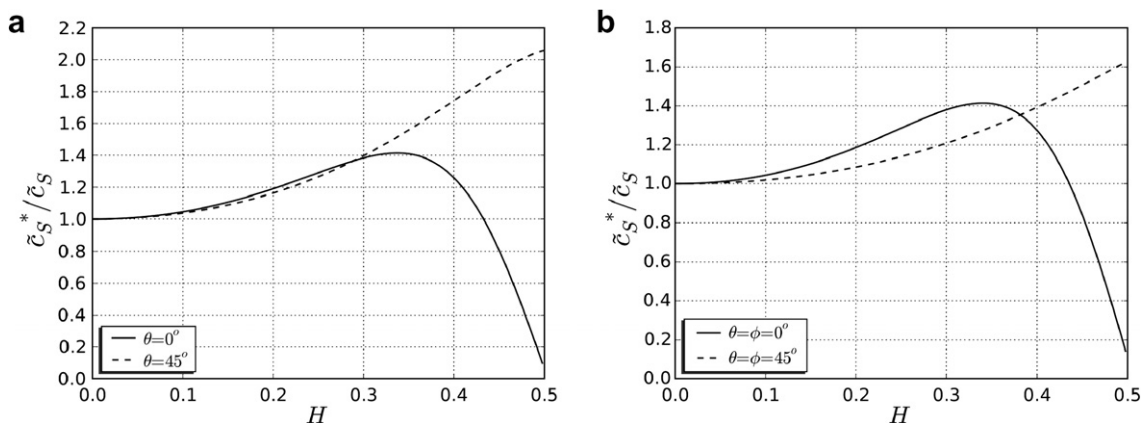

Fig. 1. 2D (a) and 3D (b) S-wave group velocity dispersion coefficients $\tilde{c}_S^*/\tilde{c}_S$ for the linear finite element method with $v = 0.1$.
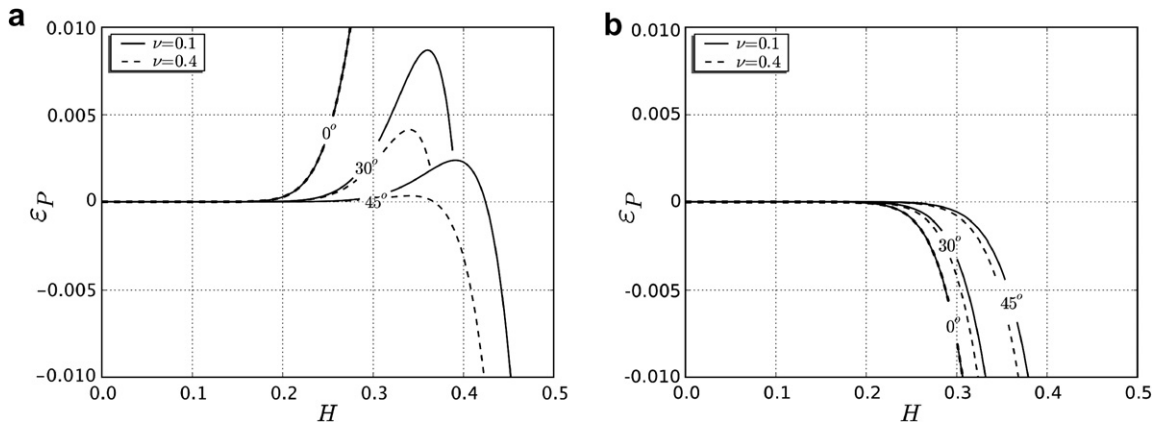
Fig. 2. 2D *P*-wave phase errors of the eighth-degree spectral element method with GLC (a) and GLL (b) collocation points.
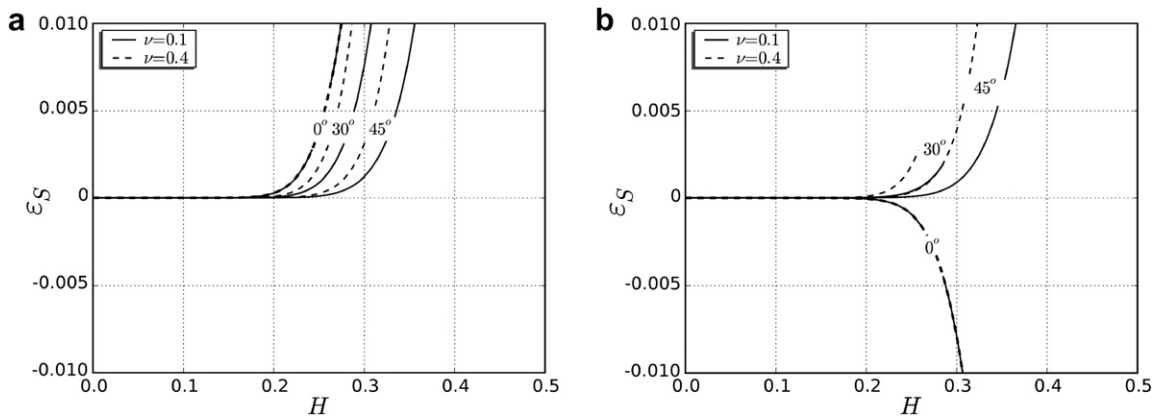

Fig. 3. 2D *S*-wave phase errors of the eighth-degree spectral element method with GLC (a) and GLL (b) collocation points.
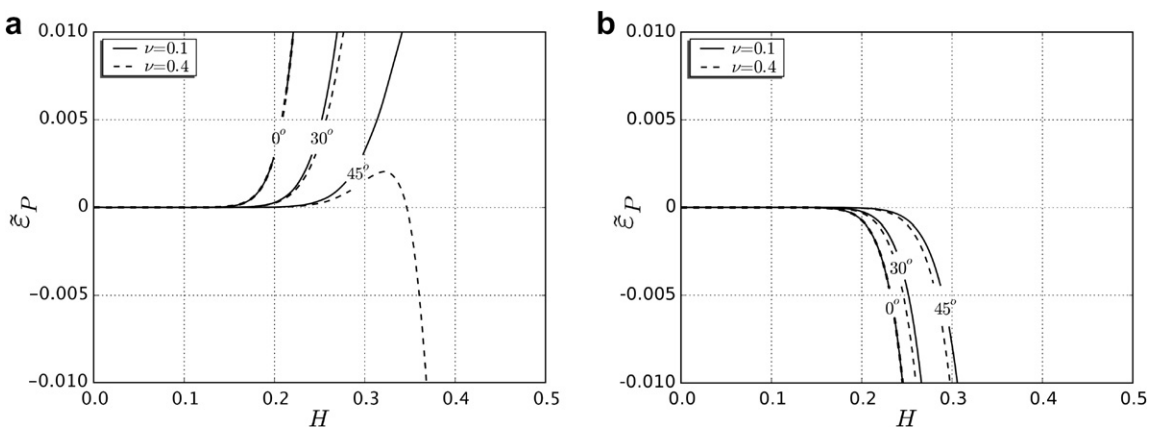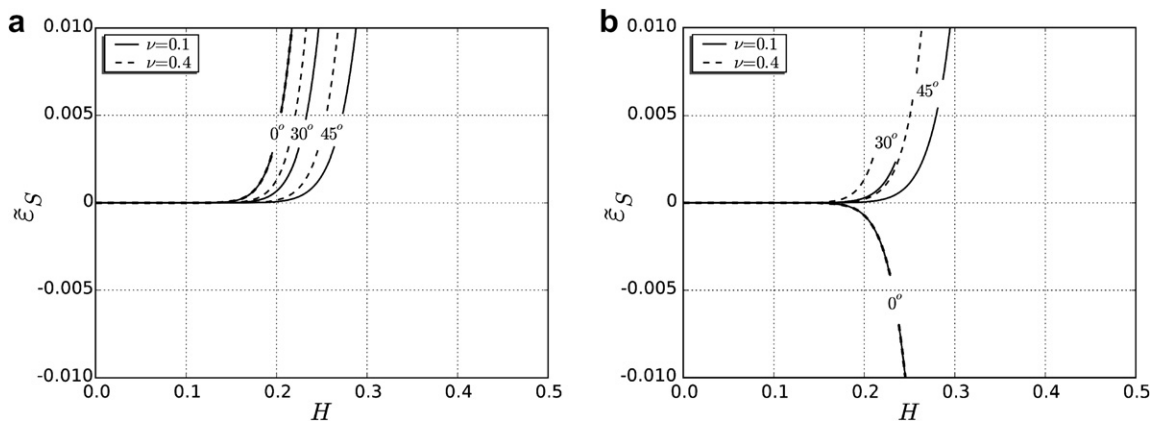

Fig. 4. 2D *P*-wave group errors of the eighth-degree spectral element method with GLC (a) and GLL (b) collocation points.

P-wave is less sensitive to changes in the Poisson's ratio at this level of accuracy. Note also that the spectral elements with GLL points are more sensitive than the ones with GLC points.

We next produce dispersion graphs of eighth-degree GLC and GLL spectral element methods with a fixed resolution of four grid points per wavelength. Figs. 11 and 12 are graphs of the phase velocity error in polar

Fig. 5. 2D S-wave group errors of the eighth-degree spectral element method with GLC (a) and GLL (b) collocation points.
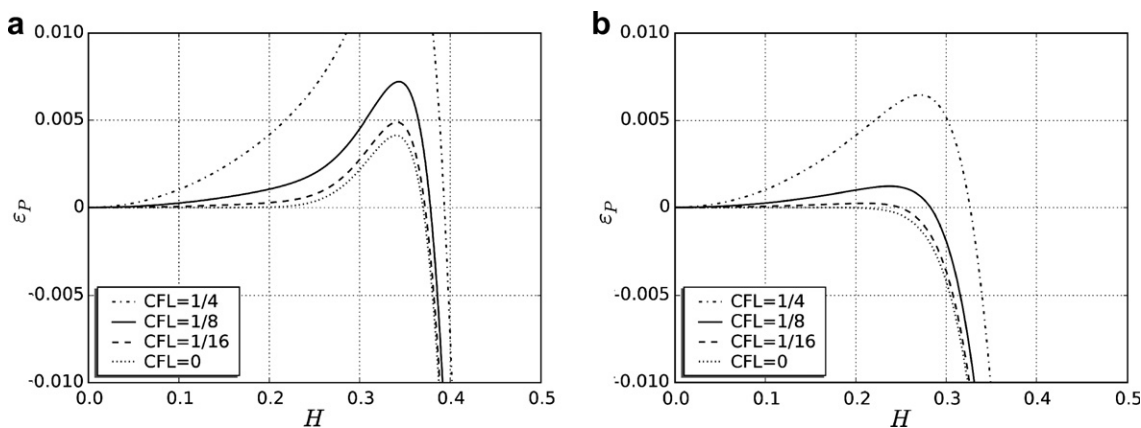
Fig. 6. 2D P-wave errors of the eighth-degree, second-order explicit in time spectral elements with GLC (a) and GLL (b) collocation points with decreasing values of the CFL ratio ($\nu = 0.4, \theta = 30°$). The time-harmonic case is indicated by CFL $= 0$.
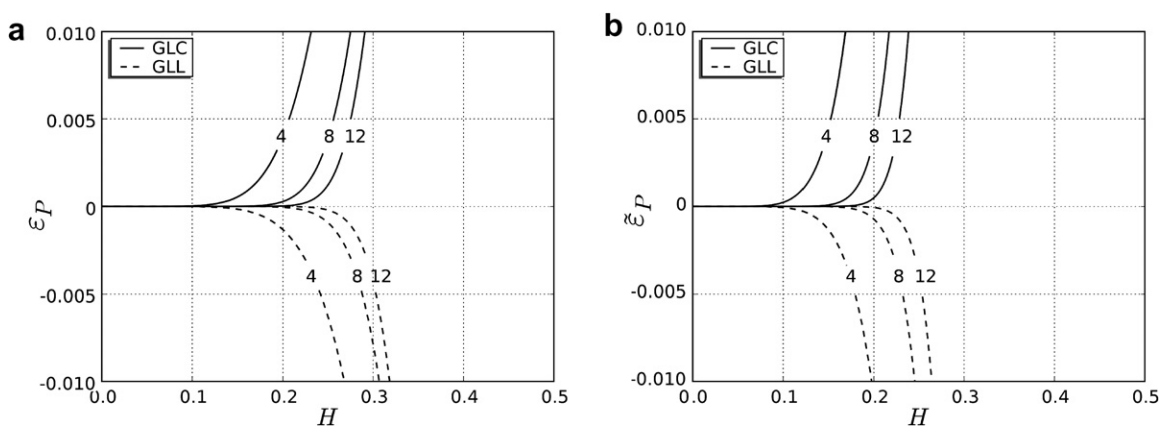
Fig. 7. 2D P-wave phase (a) and group (b) errors of the spectral element method with $N = 4, 8, 12$ and $\theta = 0°$.

coordinates. For viewing purposes, we emphasize the error by displaying the scaled phase errors $1 + 20\varepsilon_P$ and $1 + 20\varepsilon_S$ instead of ε_P and ε_S. Note that the numerical P-wave velocity is nearly insensitive to the Poisson's ratio for $G = 4$. Fig. 12 shows that both GLC and GLL methods have larger S-wave errors in the directions that make an angle of about 30° with the axes, although GLL has a higher sensitivity to the Poisson's ratio.
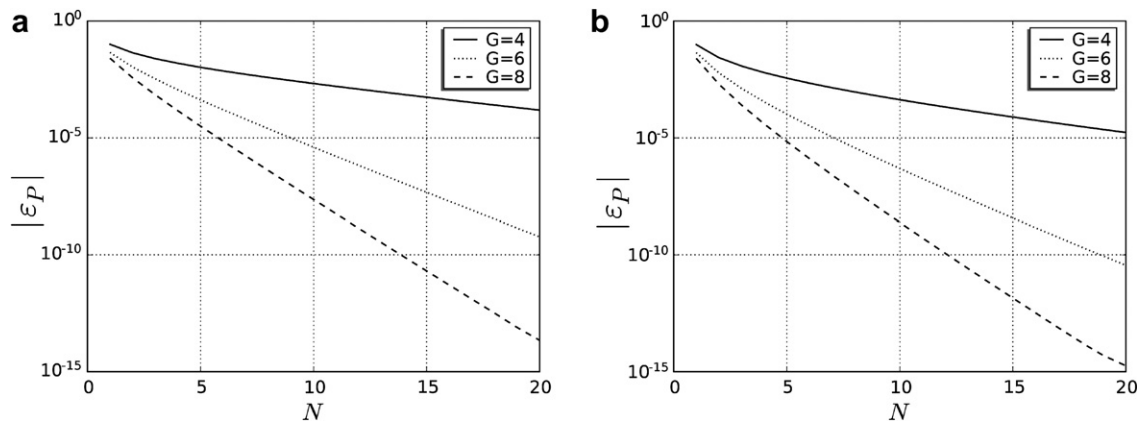
Fig. 8. 2D *P*-wave phase errors in logarithmic scale of the spectral element method with GLC (a) and GLL (b) collocation points and $\theta = 0°$.
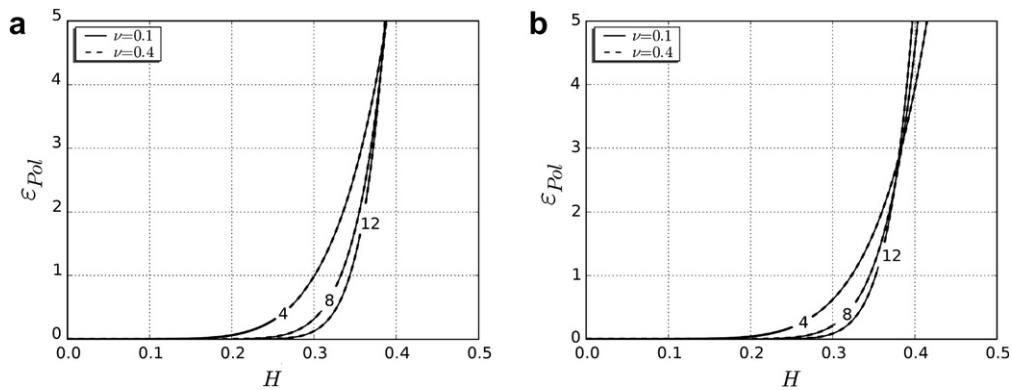

Fig. 9. Polarization errors (in degrees) of 2D spectral elements with GLC (a) and GLL (b) collocation points. We consider $\theta = 30°$.
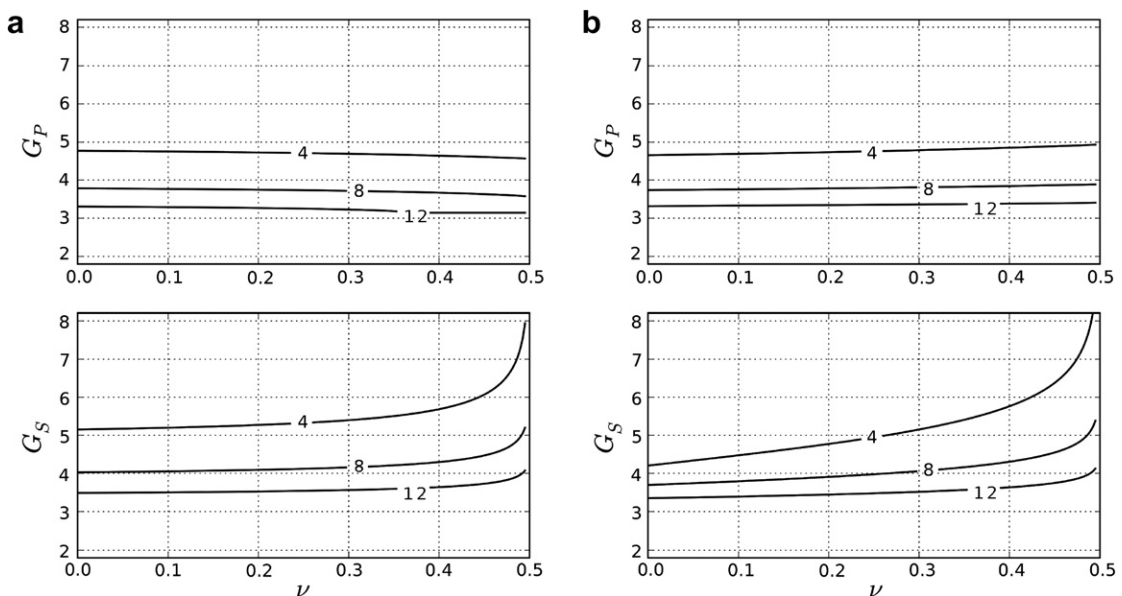

Fig. 10. Minimum number of *P*- and *S*-grid points per wavelength to keep the 2D group velocity error below 1%: GLC (a) and GLL (b) collocation points with $N = 4, 8, 12$. The direction of propagation is determined by $\theta = 30°$.
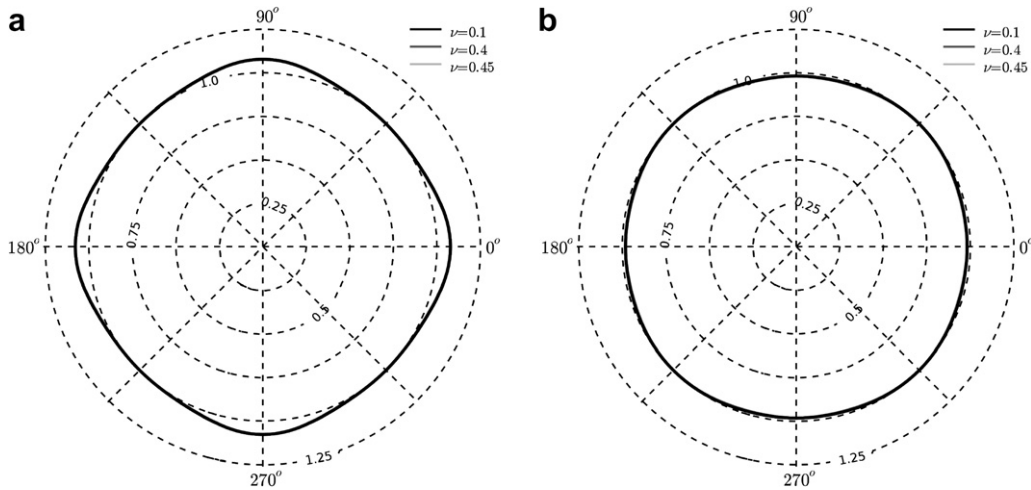
Fig. 11. 2D *P*-wave phase error in polar coordinates of the eighth-degree spectral element method with GLC (a) and GLL (b) collocation points, at four points per wavelength. The error is scaled as $1 + 20\varepsilon_P$.

Fig. 12. 2D *S*-wave phase error in polar coordinates of the eighth-degree spectral element method with GLC (a) and GLL (b) collocation points, at four points per wavelength. The error is scaled as $1 + 20\varepsilon_S$.
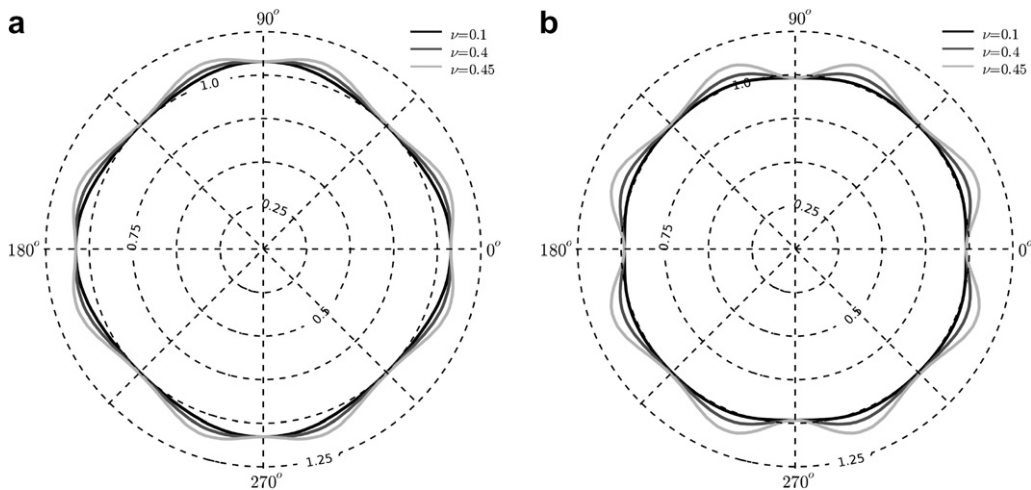
Similar results apply to the 3D case, as seen in Fig. 13, where we consider a representation of the *S*-wave phase error in spherical coordinates with the same scaling as above.

6. Conclusions

We proposed a simple dispersion analysis procedure for 2D and 3D spectral element methods for the elastic wave equation that extends known properties of linear finite elements and confirms accuracy estimates that were only experimentally known. In particular, *P*-wave dispersion and polarization errors have a lower sensitivity to the Poisson's ratio than the *S*-wave dispersion error [14], and four grid points per wavelength are sufficient to have the dispersion error below 1% on spectral element approximations of degree eight with either GLC or GLL collocation points. The presented methodology is easily extended to rectangular grids. One can also extend it to a periodic grid of non-rectangular elements as in [5].
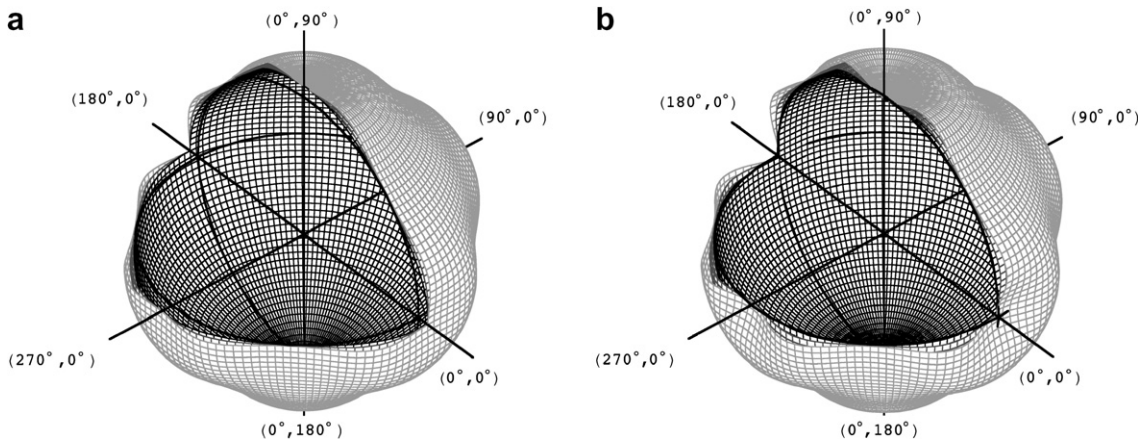
Fig. 13. 3D *S*-wave phase error in spherical coordinates of the spectral element method with GLC (a) and GLL (b) collocation points, at four points per wavelength. Light grey: $v = 0.45$; dark grey: $v = 0.4$; black: $v = 0.1$. The radius of all reference circles is one. The error is scaled as $1 + 20\varepsilon_S$.

Acknowledgements

Appendix A. 3D element matrices

The element matrices of the spectral element method for the isotropic wave equation (1) in a mesh of $h \times h \times h$ cubic elements are given by

$$
\begin{aligned}
\boldsymbol{M}^e &:= \rho \frac{h^3}{8} \boldsymbol{A} \otimes \boldsymbol{A} \otimes \boldsymbol{A}, \\
\boldsymbol{K}_1^e &:= E \frac{h}{2} \boldsymbol{A} \otimes \boldsymbol{A} \otimes \boldsymbol{B} + \mu \frac{h}{2} \boldsymbol{A} \otimes \boldsymbol{B} \otimes \boldsymbol{A} + \mu \frac{h}{2} \boldsymbol{B} \otimes \boldsymbol{A} \otimes \boldsymbol{A}, \\
\boldsymbol{K}_2^e &:= \lambda \frac{h}{2} \boldsymbol{A} \otimes \boldsymbol{C}^{\mathrm{T}} \otimes \boldsymbol{C} + \mu \frac{h}{2} \boldsymbol{A} \otimes \boldsymbol{C} \otimes \boldsymbol{C}^{\mathrm{T}}, \\
\boldsymbol{K}_3^e &:= \lambda \frac{h}{2} \boldsymbol{C}^{\mathrm{T}} \otimes \boldsymbol{A} \otimes \boldsymbol{C} + \mu \frac{h}{2} \boldsymbol{C} \otimes \boldsymbol{A} \otimes \boldsymbol{C}^{\mathrm{T}}, \\
\boldsymbol{K}_4^e &:= \mu \frac{h}{2} \boldsymbol{A} \otimes \boldsymbol{A} \otimes \boldsymbol{B} + E \frac{h}{2} \boldsymbol{A} \otimes \boldsymbol{B} \otimes \boldsymbol{A} + \mu \frac{h}{2} \boldsymbol{B} \otimes \boldsymbol{A} \otimes \boldsymbol{A}, \\
\boldsymbol{K}_5^e &:= \lambda \frac{h}{2} \boldsymbol{C}^{\mathrm{T}} \otimes \boldsymbol{C} \otimes \boldsymbol{A} + \mu \frac{h}{2} \boldsymbol{C} \otimes \boldsymbol{C}^{\mathrm{T}} \otimes \boldsymbol{A}, \\
\boldsymbol{K}_6^e &:= \mu \frac{h}{2} \boldsymbol{A} \otimes \boldsymbol{A} \otimes \boldsymbol{B} + \mu \frac{h}{2} \boldsymbol{A} \otimes \boldsymbol{B} \otimes \boldsymbol{A} + E \frac{h}{2} \boldsymbol{B} \otimes \boldsymbol{A} \otimes \boldsymbol{A}.
\end{aligned}
\tag{A.1}
$$

Appendix B. Computing the Rayleigh quotient

We present herein the details of the evaluation of the quotients d_i present in the eigenvalue problems (18) and (24). We use the following properties of the Kronecker product [12]:

$$
\begin{aligned}
(\boldsymbol{A} \otimes \boldsymbol{B})(\boldsymbol{C} \otimes \boldsymbol{D}) &= \boldsymbol{A}\boldsymbol{C} \otimes \boldsymbol{B}\boldsymbol{D}, \\
\overline{(\boldsymbol{A} \otimes \boldsymbol{B})}^{\mathrm{T}} &= \overline{\boldsymbol{A}}^{\mathrm{T}} \otimes \overline{\boldsymbol{B}}^{\mathrm{T}}.
\end{aligned}
\tag{B.1}
$$

Let us start with $d_1 = (\overline{W[\kappa]}^T K_1 W[\kappa])/(\overline{W[\kappa]}^T M W[\kappa])$ from the 2D case. We have from (7) that the restriction of $W[\kappa]$ to an element $e = e_1 + e_2 n_e$ can be written as

$$W^e[\kappa] = \exp\left(i(\kappa_1 e_1 + \kappa_2 e_2)\right) v[\kappa_2] \otimes v[\kappa_1], \quad v[\kappa_\alpha] := \left(\exp\left(i\kappa_\alpha \zeta_0 h\right), \ldots, \exp\left(i\kappa_\alpha \zeta_N h\right)\right)^T. \tag{B.2}$$

Since matrix-vector products can be carried out element by element, we have from (9) that

$$\overline{W[\kappa]}^T K_1 W[\kappa] = \sum_{e=0}^{n_e^2-1} \overline{W^e[\kappa]}^T K_1^e W^e[\kappa] = \sum_{e=0}^{n_e^2-1} \overline{W^e[\kappa]}^T (EA \otimes B + \mu B \otimes A) W^e[\kappa]. \tag{B.3}$$

In particular, it follows from (B.1) and (B.2) that

$$\overline{W^e[\kappa]}^T (A \otimes B) W^e[\kappa] = (\exp^{-i(\kappa_1 e_1 + \kappa_2 e_2)} \overline{v[\kappa_2]}^T \otimes \overline{v[\kappa_1]}^T)(A \otimes B)(\exp^{i(\kappa_1 e_1 + \kappa_2 e_2)} v[\kappa_2] \otimes v[\kappa_1])$$

$$= (\overline{v[\kappa_2]}^T \otimes \overline{v[\kappa_1]}^T)(A v[\kappa_2] \otimes B v[\kappa_1]) = (\overline{v[\kappa_2]}^T A v[\kappa_2])(\overline{v[\kappa_1]}^T B v[\kappa_1]).$$

Note that $\overline{W^e[\kappa]}^T (A \otimes B) W^e[\kappa]$ does not depend on e. Introducing the notations

$$d_\alpha^A := \overline{v[\kappa_\alpha]}^T A v[\kappa_\alpha], \quad d_\alpha^B := \overline{v[\kappa_\alpha]}^T B v[\kappa_\alpha], \quad d_\alpha^C := \overline{v[\kappa_\alpha]}^T C v[\kappa_\alpha], \tag{B.4}$$

we can write (B.3) as

$$\overline{W[\kappa]}^T K_1 W[\kappa] = \sum_{e=0}^{n_e^2-1} \left(E d_2^A d_1^B + \mu d_2^B d_1^A\right) = n_e^2 \left(E d_2^A d_1^B + \mu d_2^B d_1^A\right).$$

Analogously, we have $\overline{W[\kappa]}^T M W[\kappa] = n_e^2 (\rho h^2/4) d_2^A d_1^A$, hence

$$d_1 = \frac{n_e^2 (E d_2^A d_1^B + \mu d_2^B d_1^A)}{n_e^2 (\rho h^2/4) d_2^A d_1^A} = \frac{4}{\rho h^2}\left(E \frac{d_1^B}{d_1^A} + \mu \frac{d_2^B}{d_2^A}\right). \tag{B.5}$$

Note that the common factor n_e^2 cancels out in (B.5), thus removing the dependence on the number of elements. We follow the same steps to compute d_2 and d_3:

$$d_2 = \frac{4}{\rho h^2} \frac{\lambda \bar{d}_2^C d_1^C + \mu d_2^C \bar{d}_1^C}{d_2^A d_1^A}, \quad d_3 = \frac{4}{\rho h^2}\left(\mu \frac{d_1^B}{d_1^A} + E \frac{d_2^B}{d_2^A}\right), \tag{B.6}$$

and to compute the coefficients $d_i (i = 1, \ldots, 6)$ in the 3D case:

$$d_1 := \frac{4}{\rho h^2}\left(E \frac{d_1^B}{d_1^A} + \mu \frac{d_2^B}{d_2^A} + \mu \frac{d_3^B}{d_3^A}\right), \quad d_2 := \frac{4}{\rho h^2}\left(\lambda \frac{\bar{d}_2^C d_1^C}{d_2^A d_1^A} + \mu \frac{d_2^C \bar{d}_1^C}{d_2^A d_1^A}\right),$$

$$d_3 := \frac{4}{\rho h^2}\left(\lambda \frac{\bar{d}_3^C d_1^C}{d_3^A d_1^A} + \mu \frac{d_3^C \bar{d}_1^C}{d_3^A d_1^A}\right), \quad d_4 := \frac{4}{\rho h^2}\left(\mu \frac{d_1^B}{d_1^A} + E \frac{d_2^B}{d_2^A} + \mu \frac{d_3^B}{d_3^A}\right), \tag{B.7}$$

$$d_5 := \frac{4}{\rho h^2}\left(\lambda \frac{\bar{d}_3^C d_2^C}{d_3^A d_2^A} + \mu \frac{d_3^C \bar{d}_2^C}{d_3^A d_2^A}\right), \quad d_6 := \frac{4}{\rho h^2}\left(\mu \frac{d_1^B}{d_1^A} + \mu \frac{d_2^B}{d_2^A} + E \frac{d_3^B}{d_3^A}\right).$$

We next compute the coefficients in (B.4). Let us normalize κ_α as $\kappa_\alpha = 2\pi \mathcal{N} H_\alpha$, where $H_\alpha = 1/G_\alpha$ and G_α is the number of grid points per wavelength in the x_α direction. Note from (10) that A and B are symmetric. This implies that d_α^A and d_α^B are real and are given by

$$d_\alpha^A = \sum_{l=0}^{N} \sum_{j=0}^{N} A_{l,j} \cos \sigma_{l,j}, \quad d_\alpha^B = \sum_{l=0}^{N} \sum_{j=0}^{N} C_{l,j} \cos \sigma_{l,j}, \tag{B.8}$$

where $\sigma_{l,j} = 2\pi N H_\alpha (\zeta_j - \zeta_l)$. Taking into account that $C_{N,N} = -C_{0,0} = 1/2$, while the other entries of C satisfy $C_{i,j} = -C_{j,i}$, we have

$$d_\alpha^C = i \sum_{l=0}^{N} \sum_{j=0}^{N} C_{l,j} \sin \sigma_{l,j}. \tag{B.9}$$

Note that the coefficients d_α^C appear in (B.6) and (B.7) as real-valued products. Therefore, all coefficients d_i from the 2D and 3D analyses are real numbers.

Appendix C. Comparison with the classical dispersion analysis

Let us illustrate with some examples the classical dispersion analysis of finite element methods of degree $N > 1$ and compare it with the Rayleigh quotient approach.

Given a wave equation and the related finite element discretization, the classical analysis depends on a finite set Π of nodes such that any equation of the discrete system is identical to the equation associated to some node $x[p] \in \Pi$. We refer to the minimum set of adjacent nodes Π as the *unit cell* [7] of the mesh.

For instance, quadratic finite elements for the 1D wave equation $\ddot{u} = c^2 \Delta u$ on a homogeneous mesh yields a system that has two distinct equations, depending on whether the central node of the stencil is an element endpoint (p is even) or midpoint (p is odd):

$$(4h/15)\ddot{u}_{2k}^*(t) + (h/15)\left(\ddot{u}_{2k-1}^*(t) + \ddot{u}_{2k+1}^*(t)\right) - (h/30)\left(\ddot{u}_{2k-2}^*(t) + \ddot{u}_{2k+2}^*(t)\right) + \\ (14c^2/3h)u_{2k}^*(t) - (8c^2/3h)\left(u_{2k-1}^*(t) + u_{2k+1}^*(t)\right) + (c^2/3h)\left(u_{2k-2}^*(t) + u_{2k+2}^*(t)\right) = 0, \quad p = 2k, \tag{C.1}$$

$$(8h/15)\ddot{u}_{2k+1}^*(t) + (h/15)(\ddot{u}_{2k}^*(t) + \ddot{u}_{2k+2}^*(t)) + (16c^2/3h)u_{2k+1}^*(t) - (8c^2/3h)(u_{2k}^*(t) + u_{2k+2}^*(t)) = 0, \quad p = 2k+1. \tag{C.2}$$

In this case, the unit cell is $\Pi = \{x[2k], x[2k+1]\}$, with k arbitrary (Fig. C.1). Moreover, if u^* is in the form $u_p^*(t) = \exp(-\mathrm{i}(\omega^* t - \kappa x[p]))$, we may not find ω^* satisfying both Eqs. (C.1) and (C.2); that is, the plane wave cannot be propagated through the lattice defined by (C.1) and (C.2) in general. On the other hand, one may consider a solution with non-constant, periodic amplitude:

$$u_p^*(t) := R_p \exp(-\mathrm{i}(\omega^* t - \kappa x[p])), \quad R_p = \begin{cases} R_1, p = 2k \\ R_2, p = 2k+1. \end{cases} \tag{C.3}$$

Let $W_p = \exp(\mathrm{i}\kappa x[p])$ and $\chi = (\omega^*/c)^2$. Substituting (C.3) into (C.1),(C.2) and dividing both equations by $c^2 \exp(-\mathrm{i}(\omega^* t - \kappa x[p]))$, we find the eigenvalue problem $\widetilde{K}v = \chi \widetilde{M}v$,

$$v = \begin{bmatrix} R_1 \\ R_2 \end{bmatrix}, \quad \widetilde{M} = \frac{h}{15} \begin{bmatrix} 3 + 2\sin^2(\kappa h/2) & 2\cos(\kappa h/2) \\ 2\cos(\kappa h/2) & 8 \end{bmatrix}, \quad \widetilde{K} = \frac{4}{3h} \begin{bmatrix} 4 - \sin^2(\kappa h/2) & -4\cos(\kappa h/2) \\ -4\cos(\kappa h/2) & 4 \end{bmatrix}.$$

The solution of this eigenvalue problem yields two angular frequencies, which are associated to the *acoustical* and *optical* branches [26]:

$$\left(\frac{\omega^* h}{2c}\right)^2 = \frac{13 + 2\cos(4\pi H) \pm \sqrt{113 + 112\cos(4\pi H) + 11\sin^2(4\pi H)}}{3 - \cos(4\pi H)}, \quad H = \frac{1}{G} = \frac{\kappa(h/2)}{2\pi}. \tag{C.4}$$

Let us now consider 2D quadratic finite elements for the elastic equation (1). We begin by determining the unit cell over the patch of four elements shown in Fig. C.2. The (nine) nodes of one element are sufficient to span all equations, but we can select a smaller set. Following [15], we note that the lower left corner node 1 of element "a" is also the lower right corner node 3 of element "b", the upper right corner node 9 of element "c", and the upper left corner node 7 of element "d". Thus, the global nodes 13, 15, 23 and 25 yield the same equation in an unbounded medium and only one of them (say node 13) is needed in the unit cell. Analogously, the left midside node 4 of element "a" is also the right midside node 6 of element "b", thus only one node (say node 18) is selected for the unit cell, and so on. This arguments yield the unit cell $\Pi = \{x[13], x[14], x[18], x[19]\}$.

Consider as in (C.3) an approximate solution in the form

$$(u_\alpha^*)_p(t) = R_\alpha^*(x[p]) \exp\left[\mathrm{i}(\kappa \cdot x[p] - \omega^* t)\right]. \tag{C.5}$$

Fig. C.1. Homogeneous mesh of quadratic elements. The marked (circled) vertices compose a unit cell.
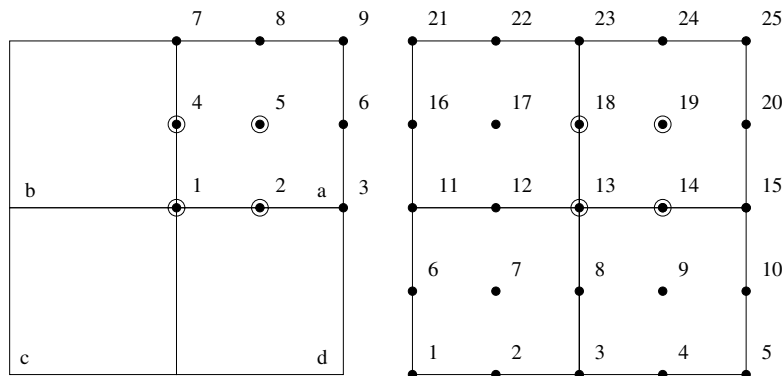
Fig. C.2. Local and global numbering on a patch of four quadratic elements. The marked vertices compose a unit cell of the unbounded grid.

Let $\chi = (\omega^*)^2$. Substituting (C.5) into (8) and dividing by $\exp(-i\omega^* t)$, we find

$$\begin{cases} \boldsymbol{K}_1 \boldsymbol{W}_1 + \boldsymbol{K}_2 \boldsymbol{W}_2 = \chi \boldsymbol{M} \boldsymbol{W}_1 \\ \boldsymbol{K}_2^{\mathrm{T}} \boldsymbol{W}_2 + \boldsymbol{K}_3 \boldsymbol{W}_2 = \chi \boldsymbol{M} \boldsymbol{W}_2, \end{cases} \quad (W_\alpha)_p := R_\alpha^*(\boldsymbol{x}[p]) \exp^{i\boldsymbol{\kappa} \cdot \boldsymbol{x}[p]}. \tag{C.6}$$

We now restrict the equations to the unit cell. Define

$$R_{\alpha,1}^* := R_\alpha^*(\boldsymbol{x}[13]), \quad R_{\alpha,2}^* := R_\alpha^*(\boldsymbol{x}[14]), \quad R_{\alpha,3}^* := R_\alpha^*(\boldsymbol{x}[18]), \quad R_{\alpha,4}^* := R_\alpha^*(\boldsymbol{x}[19]),$$

and $\Pi_j := \{k \in \{1, \ldots, 25\}; R_\alpha^*(\boldsymbol{x}[k]) = R_{\alpha,j}^*\}$. Assuming that the periodicity of $R_\alpha^*(\boldsymbol{x}[p])$ is determined by Π, we have that (C.6) reduces to the 8×8 eigenvalue problem

$$\begin{cases} \widetilde{\boldsymbol{K}}_1 \boldsymbol{v}_1 + \widetilde{\boldsymbol{K}}_2 \boldsymbol{v}_2 = \chi \widetilde{\boldsymbol{M}} \boldsymbol{v}_1 \\ \widetilde{\boldsymbol{K}}_2^{\mathrm{T}} \boldsymbol{v}_1 + \widetilde{\boldsymbol{K}}_3 \boldsymbol{v}_2 = \chi \widetilde{\boldsymbol{M}} \boldsymbol{v}_2 \end{cases} \quad \boldsymbol{v}_\alpha = (R_{\alpha,1}^*, R_{\alpha,2}^*, R_{\alpha,3}^*, R_{\alpha,4}^*),$$

$$\widetilde{M}_{i,j} = \sum_{k \in \Pi_j} M_{i,k} \exp^{i\boldsymbol{\kappa} \cdot \boldsymbol{x}_k}, \quad (\tilde{K}_l)_{i,j} = \sum_{k \in \Pi_j} (K_l)_{i,k} \exp^{i\boldsymbol{\kappa} \cdot \boldsymbol{x}_k} \quad (1 \leqslant l \leqslant 3), \qquad 1 \leqslant i \leqslant 4. \tag{C.7}$$

We refer to [8] for details on the solution to (C.7) with arbitrary polynomial degree and direction of propagation. In the particular case $\boldsymbol{\kappa} = (\kappa, 0)$, the eigenvalues of (C.7) yield the phase velocities

$$c_j^* = \frac{\omega^*}{\kappa} = \frac{\sqrt{a_j}}{2\pi H \sqrt{\rho(6 - 2\cos(4H\pi))}} \quad (j = 1, \ldots, 8),$$

$$a_{1,2} = 90E + (4\mu - 30E)\cos(4H\pi) + \mu(26 \pm \sqrt{474 + 448\cos(4H\pi) - 22\cos(8H\pi)}),$$

$$a_{3,4} = \mu(26 + 4\cos(4H\pi) \pm \sqrt{474 + 448\cos(4H\pi) - 22\cos(8H\pi)}), \tag{C.8}$$

$$a_{5,6} = E(26 + 4\cos(4H\pi) \pm \sqrt{474 + 448\cos(4H\pi) - 22\cos(8H\pi)}),$$

$$a_{7,8} = 90\mu + (4E - 30\mu)\cos(4H\pi) + E(26 \pm \sqrt{474 + 448\cos(4H\pi) - 22\cos(8H\pi)}).$$

We compare these propagation modes with the Rayleigh quotient approximation in Fig. C.3. Note that the modes predicted by the classical analysis must be switched to define the P- and S-wave propagation at coarser grids [15], while Rayleigh quotients follow the modes which are closer to the exact modes of propagation. In particular, the "best" mode changes at $H \approx 0.25$ and Rayleigh quotients are sensitive to this change (see also [6, Fig. 3]). The same applies to higher polynomial degrees, as reported in the acoustic case in [23,24]. Moreover, both analyses provide similar estimates for the admissible domain $\Gamma = [0, H_{max}]$ of the dispersion error, where $1/H_{max}$ is the minimum number of grid points per wavelength needed in order to have negligible numerical dispersion. Rayleigh quotients do depart from eigenvalues for $H > 0.3$, but an exact dispersion estimate in such a zone (where numerical waves are already dispersive) is irrelevant to our purposes. In general, the classical analysis of 1D and low-order 2D finite elements is quite simple, but becomes too complicated when the
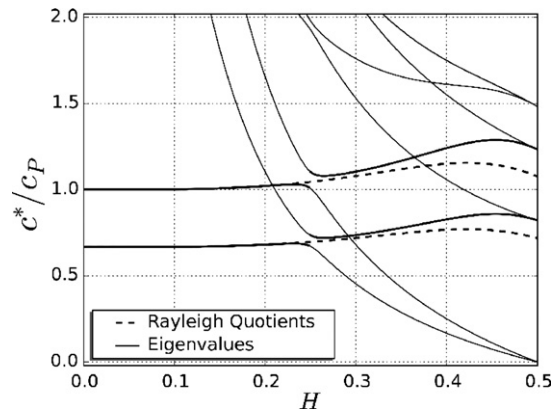
Fig. C.3. Numerical phase velocities estimated from classical dispersion analysis (solid lines) and Rayleigh quotient (dashed lines). We normalize all estimates by the exact *P*-wave velocity and set $\mu = 0.1$ and $\theta = 0°$.

dimensions of the equations and the order of the elements increase (see [[1, Appendix], for instance). Few authors have managed to produce dispersion curves of 2D spectral element methods. However, they adopted a simplified technique in which only one eigenvalue (or two, in the elastic case) is considered, while the others are discarded [5,7,8]. One can avoid neglecting higher modes of propagation by a static condensation approach [26], but we are not aware of its usage in 2D/3D problems. Furthermore, there is not a consensus on the physical meaning of the higher modes of propagation [15,17].

For practical computational purposes, the sought dispersion estimator must be easily attainable for 1D, 2D, and 3D finite elements of any order. Classical analysis has not yet delivered such an estimator. Note that the solution of eigenvalue problems in the form (C.7) also implies a high computational cost in the numerical dispersion estimates. For instance, a 3D SEM of degree 12 would imply solving an eigenvalue problem of size $3 \times 12^3 = 5184$.

The final goal of the dispersion analysis for the numerical error assessment is to determine the admissible domain of the dispersion error, in particular the optimal number of grid points per wavelength leading to an efficient and accurate numerical simulation of wave propagation. In this sense, we are not interested in exactly retrieving all the spectrum of the discrete wave operator. On the contrary, we aim to correctly estimate the part of the spectrum where the numerical dispersion generated by discretization is almost negligible with respect to a given error tolerance.

The Rayleigh quotient approach, based on the best approximation of the eigenvalues in the Ritz-Galerkin sense [10], avoids the need of neglecting extra modes regardless of the spatial dimension and yields an efficient error estimator that provides all information needed for a correct dispersion analysis. From this point of view, the results of the method are consistent with both the classical analysis and numerical experiments, and confirm the validity of our approach, motivating the departure from the classical one.

The classical technique is still necessary in other contexts such as the computation of vibrational modes of a discrete system, but one must keep in mind that it does not tell the whole story about discretization error. The eigenvectors of the discrete system, which also provide relevant information about numerical dispersion [17], should also be taken in account in a fully general analysis.

References

[1] N. Abboud, P. Pinsky, Finite element dispersion analysis for the three-dimensional second-order scalar wave equation, Int. J. Numer. Methods Eng. 35 (6) (1992) 1183–1218.
[2] C. Canuto, M. Hussaini, A. Quarteroni, T. Zang, Spectral Methods in Fluid Dynamics, Springer-Verlag, New York, NY, 1987.
[3] E. Chaljub, D. Komatitsch, J.-P. Vilotte, Y. Capdeville, B. Valette, G. Festa, Spectral element analysis in seismology, in: R.-S. Wu, V. Maupin (Eds.), Advances in Wave Propagation in Heterogeneous Media, Advances in Geophysics, vol. 48, Elsevier, 2007, pp. 365–419.

[4] M. Christon, The influence of the mass matrix on the dispersive nature of the semi-discrete, second-order wave equation, Comput. Methods Appl. Mech. Eng. 173 (1–2) (1999) 147–166.

[5] G. Cohen, Higher-Order Numerical Methods for Transient Wave Equations, Springer-Verlag, New York, NY, 2002.

[6] J. Cottrell, T. Hughes, A. Reali, G. Sangalli, Isogeometric discretizations in structural dynamics and wave propagation, in: ECCOMAS Thematic Conference on Computational Methods in Structural Dynamics and Earthquake Engineering, Rethymno, Greece, 2007.

[7] W. Dauksher, A. Emery, Accuracy in modeling the acoustic wave equation with Chebyshev spectral finite elements, Finite Elem. Anal. Des. 26 (2) (1997) 115–128.

[8] J. De Basabe, M. Sen, Grid dispersion and stability criteria of some common finite difference and finite element methods for acoustic and elastic wave propagation, in: SEG Annual Meeting, San Antonio, TX, 2007.

[9] A. Eringen, E. Suhubi, Elastodynamics, vol. 2, Academic Press, New York, NY, 1975.

[10] M.E. Hochstenbach, H.A. van der Vorst, Alternatives to the Rayleigh quotient for the quadratic eigenvalue problem, SIAM J. Sci. Comput. 25 (2) (2003) 591–603.

[11] D. Komatitsch, J. Tromp, Introduction to the spectral-element method for 3-D seismic wave propagation, Geophys. J. Int. 139 (3) (1999) 806–822.

[12] H. Lütkepohl, Handbook of Matrices, John Wiley & Sons, Chichester, UK, 1996.

[13] Y. Maday, E.M. Rønquist, Optimal error analysis of spectral methods with emphasis on non-constant coefficients and deformed geometries, Comput. Methods Appl. Mech. Eng. 80 (1–3) (1990) 91–115.

[14] K. Marfurt, Accuracy of finite-difference and finite-element modeling of the scalar and elastic wave equations, Geophysics 49 (5) (1984) 533–549.

[15] K. Marfurt, Appendix – analysis of higher order finite-element methods, in: K. Kelly, K. Marfurt (Eds.), Numerical Modeling of Seismic Wave Propagation, Geophysics Reprint Series, Soc. Expl. Geophys., vol. 13, Tulsa, OK, 1990, pp. 516–520.

[16] E.D. Mercerat, J.P. Vilotte, F.J. Sanchez-Sesma, Triangular spectral element simulation of two-dimensional elastic wave propagation using unstructured triangular grids, Geophys. J. Int. 166 (2) (2006) 679–690.

[17] W. Mulder, Spurious modes in finite-element discretizations of the wave equation may not be all that bad, Appl. Numer. Math. 30 (4) (1999) 425–445.

[18] R. Nickalls, A new approach to solving the cubic: Cardan's solution revealed, Math. Gazette 77 (480) (1993) 354–359.

[19] E. Padovani, E. Priolo, G. Seriani, Low- and high-order finite element method: Experience in seismic modeling, J. Comput. Acoust. 2 (1994) 371–422.

[20] A. Patera, A spectral element method for fluid dynamics: laminar flow in a channel expansion, J. Comput. Phys. 54 (3) (1984) 468–488.

[21] E. Priolo, J. Carcione, G. Seriani, Numerical simulation of interface waves by high-order spectral modeling techniques, J. Acoust. Soc. Am. 95 (2) (1994) 681–693.

[22] G. Seriani, A parallel spectral element method for acoustic wave modeling, J. Comput. Acoust. 5 (1) (1997) 53–69.

[23] G. Seriani, S.P. Oliveira, Optimal blended spectral element operators for forward modeling, Geophysics 72 (5) (2007) SM95–SM106.

[24] G. Seriani, S.P. Oliveira, DFT modal analysis of spectral element methods for acoustic wave propagation, J. Comput. Acoust., accepted for publication.

[25] G. Seriani, E. Priolo, Spectral element method for acoustic wave simulation in heterogeneous media, Finite Elem. Anal. Des. 16 (3–4) (1994) 337–348.

[26] L. Thompson, P. Pinsky, Complex wavenumber Fourier analysis of the p-version finite element method, Comput. Mech. 13 (4) (1994) 255–275.

[27] F. Zyserman, P. Gauzellino, Dispersion analysis of a nonconforming finite element method for the three-dimensional scalar and elastic wave equations, Finite Elem. Anal. Des. 41 (13) (2005) 1309–1326.

[28] F. Zyserman, P. Gauzellino, J. Santos, Dispersion analysis of a non-conforming finite element method for the Helmholtz and elastodynamics equations, Int. J. Numer. Methods Eng. 58 (9) (2003) 1381–1395.